Carbon 213 (2023) 118192

Contents lists available at ScienceDirect

Carbon

journal homepage: www.elsevier.com/locate/carbon

Engineering single-atom Fe–N active sites on hollow carbon spheres for oxygen reduction reaction

Rui S. Ribeiro [a,b,1,*], Ana Luísa S. Vieira [a,b,1], Krzysztof Biernacki [a,b], Alexandre L. Magalhães [c], Juan J. Delgado [d,e], Rafael G. Morais [a,b], Natalia Rey-Raap [f], Raquel P. Rocha [a,b], M. Fernando R. Pereira [a,b,**]

[a] LSRE-LCM - Laboratory of Separation and Reaction Engineering – Laboratory of Catalysis and Materials, Faculty of Engineering, University of Porto, Rua Dr. Roberto Frias, 4200-465, Porto, Portugal
[b] ALiCE - Associate Laboratory in Chemical Engineering, Faculty of Engineering, University of Porto, Rua Dr. Roberto Frias, 4200-465, Porto, Portugal
[c] LAQV/Requimte, Departamento de Química e Bioquímica, Faculdade de Ciências da Universidade do Porto, Rua do Campo Alegre, s/n, 4169-007, Porto, Portugal
[d] IMEYMAT: Institute of Research on Electron Microscopy and Materials, University of Cádiz, E11510 Puerto Real, Cádiz, Spain
[e] Departamento de Ciencia de Materiales, Ingeniería Metalúrgica y Química Inorgánica, University of Cádiz, E11510 Puerto Real, Cádiz, Spain
[f] Instituto de Ciencia y Tecnología del Carbono, INCAR-CSIC, Francisco Pintado Fe 26, 33011, Oviedo, Spain

ARTICLE INFO

Keywords:
ORR
Single-atomic catalysts
Electrocatalysis
Density-functional theory (DFT)
Fuel cells

ABSTRACT

Seeking alternatives to noble metals-based electrocatalysts for oxygen reduction reaction (ORR), hollow carbon spheres (CSs) were finely tuned with stable single-atom Fe–N species through a synthesis methodology requiring only earth-abundant metal precursors. CSs with different sizes were synthesized by sol-gel polycondensation of resorcinol with formaldehyde over silica nanoparticles, followed by thermal annealing and silica etching. A catalyst screening revealed the positive impact of both the hollow core and structural defects of the CSs for ORR. Single-atom Fe–N active sites were introduced on the best performing CSs through simultaneous incorporation of iron and nitrogen precursors, and glucose. A significant enhancement in ORR activity was observed despite the small iron load introduced (0.12 wt%). ORR performance indicators, advanced characterization, and molecular simulation studies revealed nitrogen's crucial role in anchoring individual iron atoms and modulating the charge density nearby the active sites (increase of 80 mV in the half-wave potential). Adding glucose as a chelating agent enhances the metal-heteroatom coordination and subsequent dispersion of iron, accounting for an increase of 20 mV in the half-wave potential, an average of electrons transferred as high as 3.9 (at 0.4 V *vs.* RHE), and higher stability (99%) than that of a platinum-based (20 wt%) electrocatalyst (92%).

1. Introduction

Oxygen reduction reaction (ORR) is the bottleneck of fuel cells' operation. In particular, the elementary electrochemical reaction of O_2 dissociation (*i.e.*, bond cleavage) during ORR is very challenging due to the extremely strong O = O bond (498 kJ mol^{-1}) [1–3]. As consequence, ORR at the cathode has sluggish kinetics [2,3], being over 6 orders of magnitude slower than that of the hydrogen oxidation reaction at the anode [1,4]. Therefore, it is no surprise that a large amount of R&I activities focus on developing enhanced electrocatalysts for ORR [1, 4–7].

ORR electrocatalysts have been traditionally based on noble metals-containing nanoparticles supported on carbon black – mostly platinum (Pt) and its alloys [2,4,8,9]. Thus, the widespread use of the fuel cell technology has been hindered both by the scarcity (and unsustainability) of these precious metals, as well as by the major impact of their high price on the overall costs [1,4]. Accordingly, undergoing research efforts on fuel cells have been directed to the development of alternative,

* Corresponding author. LSRE-LCM - Laboratory of Separation and Reaction Engineering – Laboratory of Catalysis and Materials, Faculty of Engineering, University of Porto, Rua Dr. Roberto Frias, 4200-465, Porto, Portugal.
** Corresponding author. LSRE-LCM - Laboratory of Separation and Reaction Engineering – Laboratory of Catalysis and Materials, Faculty of Engineering, University of Porto, Rua Dr. Roberto Frias, 4200-465, Porto, Portugal.
E-mail addresses: rsribeiro@fe.up.pt (R.S. Ribeiro), fpereira@fe.up.pt (M.F.R. Pereira).
[1] These co-authors have contributed equally to the work.

https://doi.org/10.1016/j.carbon.2023.118192
Received 27 March 2023; Received in revised form 17 May 2023; Accepted 5 June 2023
Available online 8 June 2023

broadly available, cost-effective, and sustainable electrocatalysts based mostly on transition metals (*e.g.*, iron, cobalt, and nickel), metal oxides, and carbon nanomaterials such as carbon nanotubes and graphene derivatives [5–7,9–12]. Among these, single-atom catalysts have emerged as a promising area of research due to their ability to provide greater availability of active sites with higher reactivity compared to traditional supported catalysts. These innovative materials are paving the way for a new research area in catalysis [11,12]. Nevertheless, designing a synthesis approach to overcome the typical lack of stability of single-atom catalysts (*e.g.*, due to aggregation and/or sintering) remains a main challenge in the field [11,12].

At the same time, the unique properties of hollow carbon spheres (CSs), in particular the void core surrounded by a carbon shell, render these structures attractive for electrochemical applications [13]. Accordingly, G. Ferrero et al. reported hollow CSs with Fe–N active sites as good electrocatalysts for ORR [14]. Nevertheless, those CSs contained Fe nanoparticles in addition to single-atom Fe–N. More recently, C. Shu et al. reported the high ORR activity of a core-shell Fe–N–C electrocatalyst composed of a CSs core and a Fe-doped m-phenylenediamine polymerized shell [15]. Having all this in mind, the main goal of this study was to develop an alternative synthesis methodology for the design of highly active and stable hollow CSs containing only single-atom Fe–N as active sites by employing earth-abundant metal precursors. This is particularly relevant since many of the recent advances in the functionalization of carbon materials with Fe–N species result from the incorporation of expensive precursors such as phthalocyanines and porphyrins [16]. Accordingly, the metal-free CSs (both with hollow and SiO_2 core) with different sizes developed in our previous publication on environmental remediation [17] were first screened for ORR in basic media using a standard three-electrode configuration (with glassy carbon, Ag/AgCl, and carbon rod as working, reference, and counter electrodes, respectively). These materials were selected to study the effect of both size and hollow carbon structures in ORR. The best-performing hollow CSs were then selected as support for single-atom Fe–N active sites. Fe load was optimized, followed by a detailed study on the role of each synthesis precursor towards obtaining the electrocatalyst with the highest activity for ORR, including the application of advanced characterization techniques and molecular simulation tools. Cyclic voltammetry (CV), linear sweep voltammetry (LSV), and chronoamperometry measurements (in the presence and absence of methanol) were carried out. Standard operating conditions and performance indicators used to characterize the performance of electrocatalysts in ORR were considered. Additional insights on electrocatalytic active sites and ORR pathways were obtained through density functional theory (DFT) calculations.

2. Materials and methods

2.1. Chemicals and materials

The chemicals and materials employed in this study are detailed in Text S1.

2.2. Synthesis of Fe–N-doped hollow carbon spheres

Bare CSs were prepared according to the procedure reported in our previous publication [17], as detailed in Text S2 and depicted in the top section of Fig. 1. Briefly, silica (SiO_2) spheres were obtained through the Stöber's method and encapsulated within a resorcinol-formaldehyde resin subsequently carbonized at 800 °C under N_2 flow. Hollow CSs were finally obtained upon etching the SiO_2 core with NaOH. The resulting materials were denoted as CS_X, where X corresponds to the different ethanol/water volumetric ratios (2, 4.5, and 7) employed to obtain the Stöber's SiO_2 spheres. Samples obtained prior to SiO_2 etching ($SiO_2@CS_X$; cf. Fig. 1) were also considered.

CS_7 (*i.e.*, the hollow CSs prepared considering an ethanol/water volumetric ratio of 7 in the respective synthesis) were then doped with Fe and N, as depicted in the bottom section of Fig. 1. This was accomplished by adapting the procedure previously reported elsewhere [18]. Accordingly, 60 mg of CS_7 was added to an aqueous solution containing 0.05 mmol of iron (III) nitrate nonahydrate and 6.7 mmol of D-(+)-glucose. The resulting suspension was sonicated for 30 min to promote the adsorption of glucose (employed as chelating agent) on the carbon surface and the subsequent chelation of Fe ions, thus promoting physical isolation of Fe atoms. The solid product (CS_7Fe-Glucose; cf. Fig. 1) was collected by centrifugation, washed with ultrapure water, dried overnight at 60 °C, manually mixed with melamine (considering a CS_7/melamine mass ratio of 0.2), and thermally annealed under a N_2 flow (100 cm^3 min^{-1}) for 120 min at 800 °C, considering a heating rate of 10 °C min^{-1}. The resulting material was denoted as CS_7Fe–N. Additional materials were prepared in the absence of glucose ($CS_7Fe\text{-}N_{No\ glucose}$), melamine ($CS_7$Fe), and iron (III) nitrate nonahydrate (CS_7–N); and considering different Fe loadings in the respective synthesis, namely 0.3, 0.1, and 0.03 mmol ($CS_7Fe_{0.3}$-N, $CS_7Fe_{0.1}$-N, and $CS_7Fe_{0.03}$-N, respectively).

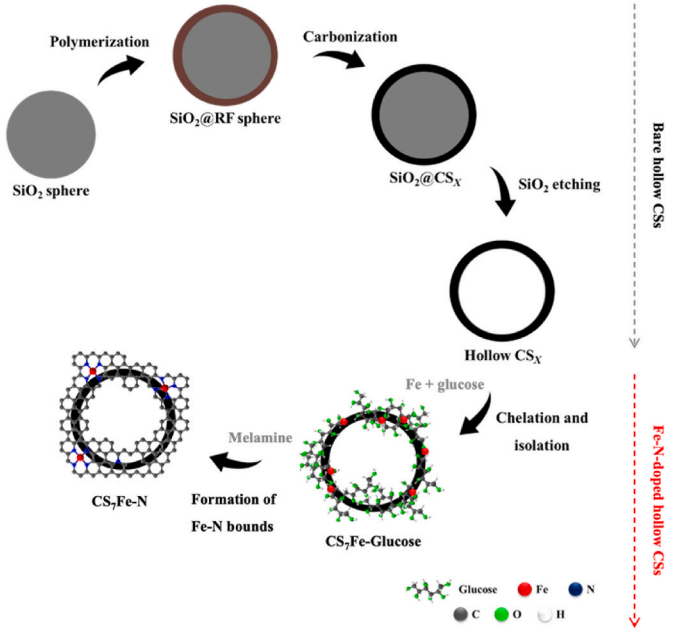

Fig. 1. Strategy employed for the design of single-atom Fe–N active sites on hollow carbon spheres (CSs), resulting in the material denoted as CS_7Fe–N. (A colour version of this figure can be viewed online.)

2.3. Characterization techniques

The characterization techniques employed in this study are detailed in Text S3. Briefly, N_2 physisorption, scanning electron microscopy (SEM) coupled with energy-dispersive X-ray spectroscopy (EDS), and X-ray diffraction (XRD) were performed as previously described [17]. Likewise, the procedures used to obtain X-ray photoelectron spectroscopy (XPS) [19] and Raman [20] spectra were also described in our previous publications. The ash residue was determined by thermogravimetric analysis (TGA). The bulk content of Fe in the CSs was determined by inductively coupled plasma – optical emission spectrometry (ICP-OES) analysis of the solution resulting from the acidic digestion of the solids, by adapting the procedure previously reported [19]. Electrical conductivity was determined by adapting the four-point probe methodology previously reported [21]. High resolution High Angle Annular Dark Field Scanning Transmission Electron Microscopy (HAADF-STEM) imaging was performed on a double aberration corrected (AC), monochromated, FEI Titan3 Themis 60–300 microscope

operated at 200 kV. Please refer to Text S3 for additional details.

2.4. Electrochemical measurements

A mixture containing 4 mg of CSs, 80 μL of Nafion perfluorinated resin solution, 80 μL of absolute ethanol, and 470 μL of ultrapure water was sonicated for 30 min. A calculated volume of the resulting suspension was then drop-casted on the glassy carbon working electrode (dried at room temperature) to obtain a catalyst load of 0.3 mg cm^{-2} on the electrode surface. All electrochemical measurements were performed on the carbon modified electrodes, as detailed in our previous publication [20] and in Text S4. Briefly, the CSs were incorporated in the working electrode through the drop-casting method and tested in ORR (basic media; 0.1 mol L^{-1} KOH) using a standard three-electrode configuration: Ag/AgCl reference electrode; glassy carbon rod counter electrode; and, as working electrode, a rotating ring-disc electrode with a glassy carbon disc and a platinum ring, or a glassy carbon rotating disc electrode. Cyclic voltammetry (CV), linear sweep voltammetry (LSV), and chronoamperometry measurements were carried out. Common indicators used to characterize the performance of electrocatalysts in ORR were determined from experiments performed in triplicate with a rotation speed of 1600 rpm: onset potential (E_{onset}; defined as the potential needed to achieve a current density of 0.1 mA cm^{-2}); half-wave potential ($E_{1/2}$; defined as the maximum of the first derivative of the current density-potential curve); limiting current density (J_L; defined as the current density at 0.2 V *vs*. RHE); hydrogen peroxide (H_2O_2) formation (H_2O_2 (%); Eq. S2); and average number of electrons transferred during the ORR (n_e; Eq. S3). The average values obtained from triplicate measurements are provided in Tables, whereas the individual results that most resemble the average values calculated from the triplicates are provided in Figures. The standard deviation of E_{onset}, $E_{1/2}$, J_L, H_2O_2 formation, and n_e determinations was never above 0.01 V, 0.02 V, 0.37 mA cm^{-2}, 4.6%, and 0.1, respectively.

The electrochemically active surface area (ECSA) was estimated from the double layer capacitance (C_{DL}), based on the specific capacitance of carbon black, C_S = 27.5 μF cm^{-2} (Text S4). Tafel plots were obtained from LSV data (1600 rpm) in the kinetically controlled region nearby E_{onset} and the slope was obtained by linear fitting. The exchange current density (J_0) was calculated from the Tafel slopes, as the point where the *y*-intercept equals the O_2/H_2O standard reduction potential ($E^0_{O2/H2O}$ = 1.229 V *vs*. RHE).

2.5. Molecular modeling

The possible electrocatalytic active sites on a graphene sheet and reaction pathways for ORR were examined through hybrid DFT calculations performed with Gaussian 09 software [22]. All the calculations were carried out using B3LYP/6-31G(d,p) level of theory with all atoms fully relaxed [23,24]. The solvent (water) effect was considered by the Polarizable Continuum Model (PCM) [25]. Each geometry optimization was followed by calculations of the harmonic vibrational frequencies in order to confirm that the optimized geometry corresponds to a minimum of total energy. All molecular structures corresponding to relevant minima on the potential energy surface have been studied, which correspond to intermediate states in the ORR process, as well as the reactant and product states; extra energy barriers exist but were not considered due to the unbalanced electron numbers borne by different states. Gibbs free energy for each elementary step of ORR was calculated through the computational hydrogen electrode (CHE) method [26,27]. Schematic representations of the optimized structures were produced with the GaussView 6.0 molecular visualization program [28]. Please refer to Text S5 for additional details.

3. Results and discussion

3.1. Preliminary screening of bare CSs

Both the bare hollow carbon spheres (CS_X) and those obtained prior to SiO_2 etching ($SiO_2@CS_X$) were already extensively characterized in our previous publication [17]. Characterization techniques such as N_2 physisorption, SEM-EDS, XRD, and TGA allowed confirming the suitability of the synthesis methodology to obtain hollow CSs, as well as the ability of tailoring the size of the CSs by changing the ethanol/water volumetric ratio considered in the respective synthesis (Stöber's method, as detailed in Text S2). Specifically, it was found that the sizes of CS_X increase with the ethanol/water volumetric ratio (Fig. 2a–c) [17].

Preliminary experiments were herein carried out to evaluate the performance of bare CS_X and $SiO_2@CS_X$ in ORR. Oxygen reduction humps are clearly observed in the CV curves of all the samples (Fig. 2d and e). However, some differences in peak intensities and positions are observed. The LSV curves confirm these differences (Fig. 2f and g). Indeed, the hollow CSs (*i.e.*, CS_2, $CS_{4.5}$, and CS_7) perform better than those obtained prior to SiO_2 etching (*i.e.*, $SiO_2@CS_2$, $SiO_2@CS_{4.5}$, and $SiO_2@CS_7$) regardless of the indicator considered (Table 1), suggesting the positive impact of the hollow structure for ORR. Please refer to Text S6 for additional discussion on the different performances observed among the CSs with SiO_2 cores (Fig. 2f).

Regarding the reaction mechanism, it is widely known that ORR in alkaline media can proceed through the direct four-electron pathway (Eq. (1)) or the indirect two-electron pathway (Eq. (2)); the former being preferred. Regarding the latter, subsequent reduction (Eq. (3)) or disproportionation (Eq. (4)) of peroxide ions is needed [29]. ORR mechanisms on metal-free carbon materials have been recently reviewed [1]. In this case, no significant differences in reaction mechanism are observed upon SiO_2 etching (Table 1). Indeed, n_e in the range 2.7–3.2 reveals the contribution of both the direct and indirect reaction pathways. Nevertheless, H_2O_2 formation is always lower and n_e is always higher for the hollow CSs.

$$O_2 + 2H_2O + 4e^- \rightleftharpoons 4OH^- \quad (1)$$

$$O_2 + H_2O + 2e^- \rightleftharpoons HO_2^- + OH^- \quad (2)$$

$$HO_2^- + H_2O + 2e^- \rightleftharpoons 3OH^- \quad (3)$$

$$2HO_2^- \rightleftharpoons 2OH^- + O_2 \quad (4)$$

Some differences can also be identified within the performances of the CSs (Fig. 2g and Table 1). Although E_{onset} and $E_{1/2}$ are apparently unaffected, clear trends are visible for the other indicators (Table 1). Indeed, increasingly better values of J_L, H_2O_2 formation, n_E, and stability are obtained as the ethanol/water volumetric ratio employed during the synthesis of the CSs increases, *i.e.*, the performances obtained follow the order: $CS_2 < CS_{4.5} < CS_7$. The role of textural properties and porosity of carbon materials in their ORR performances has already been reported [30,31]. However, as determined in our previous publication, CS_2 and CS_7 possess similar porosity and surface area, whereas these properties are less developed in $CS_{4.5}$ (Table S1) [17]. Therefore, at least another property of the hollow CSs is expected to contribute to the different performances obtained. Bearing that in mind, Raman spectroscopy was carried out to gain insights into structural defects and other crystal disorder of the hollow CSs. The resulting Raman spectra revealed that the intensity ratio of the D band relative to the G mode (I_D/I_G) increases as the ethanol/water volumetric ratio employed during the synthesis of the CSs increases (Fig. 2h), *i.e.*, the amount of structural defects follows the order: $CS_2 < CS_{4.5} < CS_7$. This is precisely the same trend obtained for J_L, H_2O_2 formation, n_e, and stability, suggesting that electron rich regions caused by structural defects slightly shift the ORR pathway from the indirect two-electron pathway (Eq. (2), followed by Eq. (3) and/or (4)) to the preferred direct four-electron pathway (Eq. (1)), thus yielding

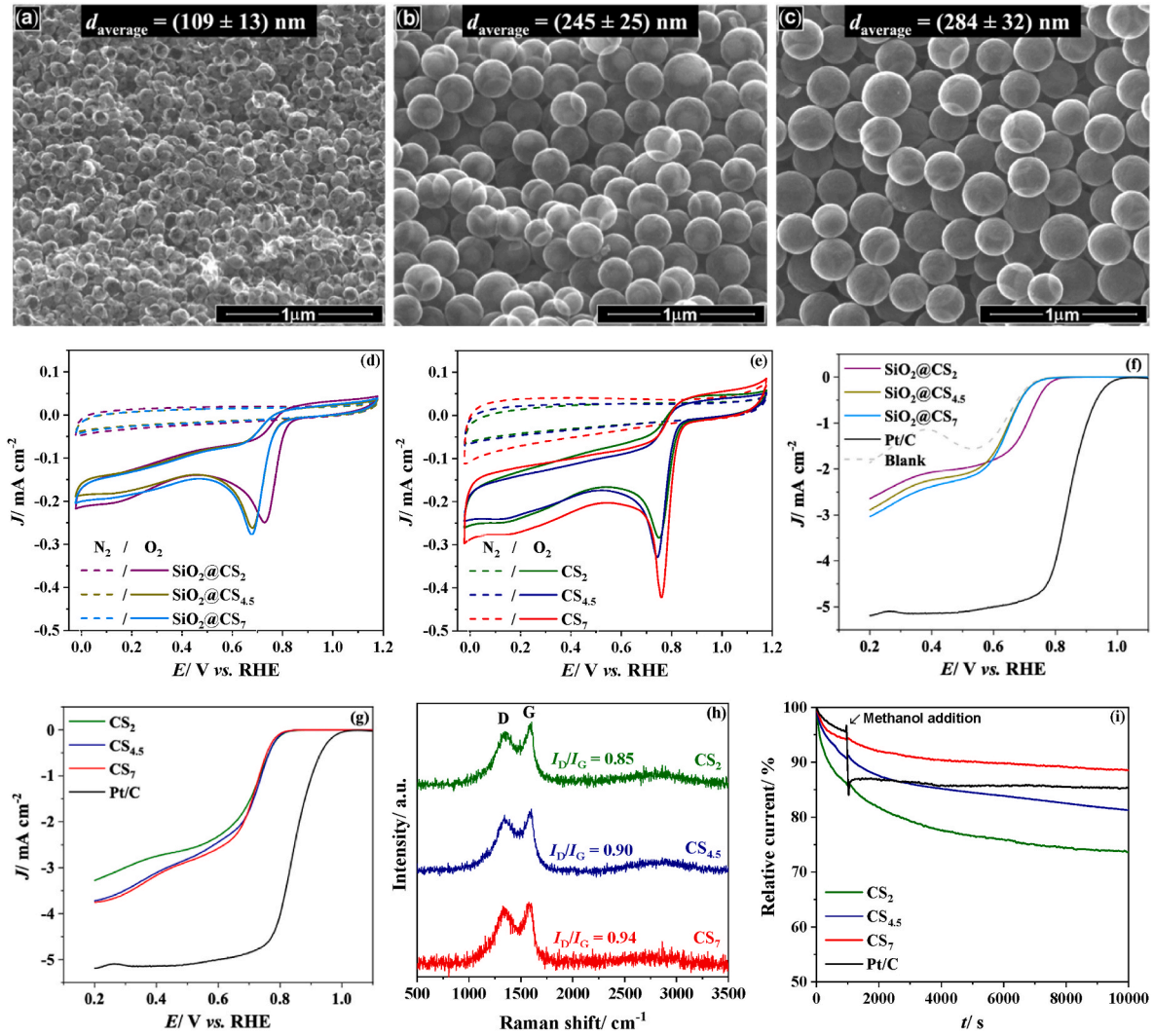

Fig. 2. Scanning electron microscopy (SEM) micrographs of (a) CS_2, (b) $CS_{4.5}$, and (c) CS_7 obtained in secondary electron detection mode; cyclic voltammetry (CV) curves of (d) SiO_2@CSs and (e) CSs series, obtained in N_2- and O_2-saturated 0.1 mol L^{-1} KOH at 5 mV s^{-1}; linear sweep voltammetry (LSV) curves of (f) SiO_2@CSs and (g) CSs series, obtained in O_2-saturated 0.1 mol L^{-1} KOH at 1600 rpm; (h) Raman spectra of the CSs; and (i) stability of CSs to methanol cross-over at 0.4 V *vs.* RHE. Results obtained with commercial Pt/C are also given in (f), (g), and (i) for comparison. Results obtained in the absence of electrocatalyst (blank) are also given in (f). Insets in (a), (b), and (c) correspond to the average diameter ($d_{average}$) as determined by SEM measurements in our previous publication [17]. (A colour version of this figure can be viewed online.)

Table 1
Summary of oxygen reduction reaction (ORR) results obtained in the preliminary screening of bare CSs: onset potential (E_{onset}), half-wave potential ($E_{1/2}$), limiting current density (J_L), hydrogen peroxide (H_2O_2) formation, number of electrons transferred (n_e), and stability[a].

Sample	E_{onset}/ V	$E_{1/2}$/ V	J_L[b]/mA cm^{-2}	H_2O_2[c]/ %	n_e[b]	Stability[d]/ %
SiO_2@CS_2	0.79	0.72	1.90	64.9	2.7	n.d.
SiO_2@$CS_{4.5}$	0.74	0.65	2.89	65.8	2.7	n.d.
SiO_2@CS_7	0.74	0.65	3.04	64.6	2.7	n.d.
CS_2	0.81	0.74	3.52	62.3	2.8	76
$CS_{4.5}$	0.80	0.73	3.76	45.5	3.1	83
CS_7	0.81	0.74	3.88	41.7	3.2	89
Pt/C	0.98	0.84	5.10	2.5	3.9	92

[a] All data refers to experiments performed at 1600 rpm.
[b] Calculated at 0.2 V *vs.* RHE.
[c] Calculated at 0.4 V *vs.* RHE.
[d] Calculated after 10000 s at 0.4 V *vs.* RHE; n.d.: not determined.

increasingly higher J_L values and stability. Indeed, defects in graphene sheets have already been reported as intrinsically active sites towards ORR, the activity resulting mainly from zigzag edges and the oxygen-containing groups on zigzag edges of graphene sheets [1,32]. Therefore, the ORR performance obtained with the bare hollow CSs can be ascribed to their defective structure (Raman I_D/I_G ratios in the range 0.85–0.94; Fig. 2h)

Overall, the activity of the best-performing metal-free CSs in ORR (*i.e.*, CS_7) is still far from that obtained with the commercial noble-metal containing Pt/C (Fig. 2g and Table 1). Nevertheless, CS_7 reveals a stability to methanol cross-over significantly higher than that of Pt/C (Fig. 2i). In fact, no differences are observed in the stability obtained with CS_7 during 10000 s at 0.4 V *vs.* RHE in the absence (11%, cf. Table 1) and presence (11%, cf. Fig. 2i) of methanol, whereas the relative current yielded by Pt/C decreases an additional 7% when methanol is added (from 8 to 15% stability loss, cf. Table 1 and Fig. 2i, respectively). Resistance to methanol cross-over is a crucial advantage when real-scale applications are envisaged; one that will be explored in the following section upon employing CS_7 as support for Fe–N active sites.

3.2. Towards the design of single-atom Fe–N active sites

3.2.1. Optimization of Fe load

Fe–N-doped hollow CSs with varying Fe loads were prepared as depicted in Fig. 1 and detailed in Section 2.2, and employed in ORR. Similar oxygen reduction humps are clearly observed in the CV curves of the Fe–N-doped hollow CSs (Fig. 3a). However, obvious differences can be identified in both the LSV curves (Fig. 3b) and the ORR performance indicators considered (Table 2). Fe–N-doping enhances E_{onset} and $E_{1/2}$ regardless of the Fe load employed (Table 2). It also enhances J_L in all cases except for $CS_7Fe_{0.3}$-N (*i.e.*, the Fe–N-doped hollow CSs synthesized with the highest Fe load). Indeed, CS_7Fe–N yields a J_L (4.68 mA cm^{-2}) almost as high as that obtained with Pt/C (5.10 mA cm^{-2}). Likewise, Fe–N-doping decreases H_2O_2 formation from 41.7% (with CS_7) down to values in the range 4.4–7.8% and increases n_e from 3.2 (with CS_7) up to values in the range 3.8–3.9, which are similar to those obtained with Pt/C (Fig. 3c and d, and Table 2). This is a clear indication that ORR on the Fe–N-doped hollow CSs proceeds mainly through the preferred direct four-electron pathway (Eq. (1)). Moreover, the stability of the Fe–N-doped hollow CSs for ORR is always higher (in the range 98–99%) than

Table 2
Summary of ORR results obtained with CS_7 and Fe–N-doped hollow CSs: onset potential (E_{onset}), half-wave potential ($E_{1/2}$), limiting current density (J_L), hydrogen peroxide (H_2O_2) formation, number of electrons transferred (n_e), and stability[a].

Sample	E_{onset}/ V	$E_{1/2}$/ V	J_L[b]/mA cm^{-2}	H_2O_2[c]/ %	n_e[b]	Stability[d]/ %
CS_7	0.81	0.74	3.88	41.7	3.2	89
$CS_7Fe_{0.3}$-N	0.89	0.78	3.68	6.8	3.9	98
$CS_7Fe_{0.1}$-N	0.90	0.77	4.63	4.4	3.9	98
CS_7Fe–N	0.90	0.79	4.68	6.9	3.9	99
$CS_7Fe_{0.03}$-N	0.90	0.79	4.33	7.8	3.8	99
Pt/C	0.98	0.84	5.10	2.5	3.9	92

[a] All data refers to experiments performed at 1600 rpm.
[b] Calculated at 0.2 V *vs.* RHE.
[c] Calculated at 0.4 V *vs.* RHE.
[d] Calculated after 10000 s at 0.4 V *vs.* RHE.

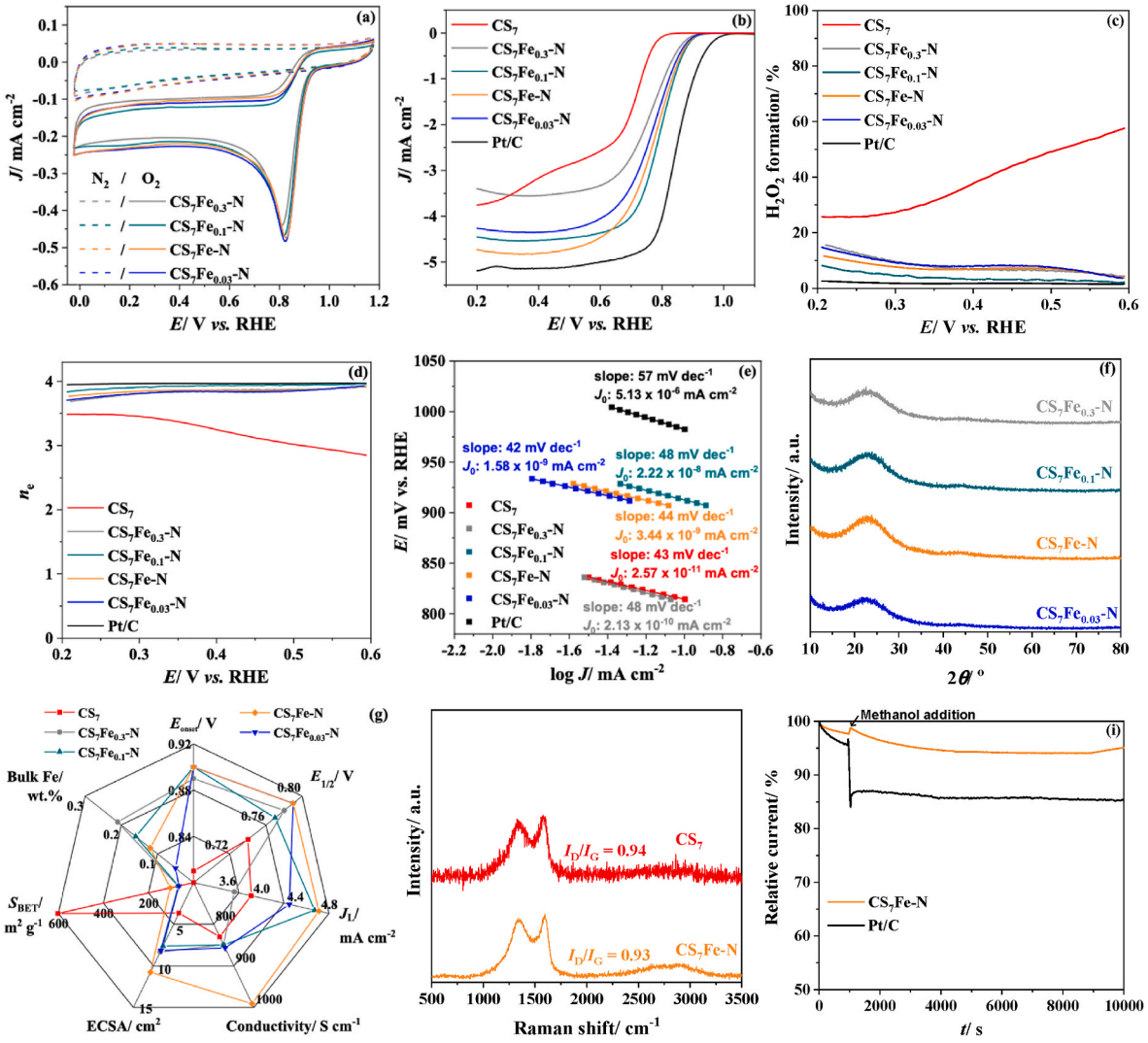

Fig. 3. (a) Cyclic voltammetry (CV) curves of the Fe–N-doped hollow CSs, obtained in N_2- and O_2-saturated 0.1 mol L^{-1} KOH at 5 mV s^{-1}; (b) linear sweep voltammetry (LSV) curves of CS_7 and Fe–N-doped hollow CSs, obtained in O_2-saturated 0.1 mol L^{-1} KOH at 1600 rpm; (c) number of electrons transferred (n_e) and (d) hydrogen peroxide (H_2O_2) formation during the experiments depicted in (b); (e) Tafel plot for CS_7 and Fe–N-doped hollow CSs; (f) X-ray diffraction (XRD) patterns of the Fe–N-doped hollow CSs; (g) radar chart comparing multiple quantitative variables; (h) Raman spectra of CS_7 and CS_7Fe–N; and (i) stability of CS_7Fe–N to methanol cross-over at 0.4 V *vs.* RHE. Results obtained with commercial Pt/C are also given in (b), (c), (d), (e), and (i) for comparison. The exchange current density (J_0) is also given in (e). (A colour version of this figure can be viewed online.)

that obtained with Pt/C (92%; Table 2), and the Tafel plot slopes are always lower (Fig. 3e). Regarding the latter, a slope of 57 mV dec^{-1} was found for Pt/C, which precisely matches the value previously reported in the literature for this commercial noble metal-containing catalyst in low current density [29]. However, Tafel slopes in the range 42–48 mV dec^{-1} were found for the CSs, indicating a slightly faster electron transfer process on these carbons [33]. Nevertheless, the Tafel slope is mostly useful to provide mechanism insights by revealing the rate determining step (RDS) of ORR [34]. Tafel slopes at *ca.* 60 mV dec^{-1} correspond to a pseudo-two-electron reduction reaction as the RDS, whereas first electron reduction of oxygen as RDS is presumed for Tafel slopes at *ca.* 120 mV dec^{-1} [35]. The Tafel slopes given in Fig. 3e are in the range 42–57 mV dec^{-1}, suggesting that the reaction rate in the low overpotential region is mainly controlled by the pseudo-two-electron reduction reaction regardless of the electrocatalyst under consideration. J_0 can also be obtained from Tafel plots, mostly useful for providing information on ORR activity. In fact, J_0 can be correlated to the constant rate of ORR [36]. J_0 values were accordingly calculated from the Tafel plots (Fig. 3e). As observed, a J_0 of 2.57 × 10^{-11} mA cm^{-2} was found for CS_7, which is 5 orders of magnitude lower than that obtained for Pt/C (5.13 × 10^{-6} mA cm^{-2}). The J_0 obtained for the Fe–N-doped hollow CSs fall between those, the two highest values being found for $CS_7Fe_{0.1}$-N (2.22 × 10^{-8} mA cm^{-2}) and CS_7Fe–N (3.44 × 10^{-9} mA cm^{-2}), *i.e.*, the two Fe-containing CSs with the best performance in ORR (Fig. 3b–d and Table 2). All these results confirm the importance of properly defining the Fe load employed during the synthesis of Fe–N-doped hollow CSs when seeking for high-performance electrocatalysts for ORR.

N_2 adsorption-desorption isotherms were collected (Fig. S1), revealing that the hollow CSs completely loose micropores upon Fe–N-doping (as observed from the negligible N_2 adsorption at low P/P_0). As shown in Table S2, the specific surface area (S_{BET}; in the range 65–111 m^2 g^{-1}) also decreases significantly when compared to that of CS_7 (602 m^2 g^{-1}), as well as the total pore volume (V_{Total}). This phenomenon may be explained by pore blockage promoted by Fe and/or glucose used for the functionalization of the hollow CSs. TGA revealed that the ash content (in the range 43–47 wt%) is unaffected by the Fe load employed during the synthesis of Fe–N-doped hollow CSs, as values close to that of CS_7 are always obtained (Table S3). As discussed in our previous publication, the ash content is explained by the presence of residual amounts of SiO_2 even after the etching process with NaOH [17]. The XRD patterns reveal no clear crystalline phases regardless of the Fe load on the hollow CSs (Fig. 3f). Only a broad peak at $2\theta \approx 23^o$ and a very slight peak at $2\theta \approx 44^o$ are observed, which are consistent with amorphous carbon and silica [37].

A radar chart comparing several variables is given in Fig. 3g, including ORR performance indicators (Table 2), S_{BET}, electrical conductivity, ECSA and bulk Fe content determined by ICP-OES (Table S3). This presentation approach clearly highlights that the performance of the Fe–N-doped hollow CSs in ORR cannot be explained by a single property, but rather by an interplay between properties. The best-performing sample, according to the values of E_{onset}, $E_{1/2}$, and J_L (*i.e.*, CS_7Fe–N), possesses the second highest S_{BET} (Fig. 3g). Despite CS_7 possessing a much larger S_{BET}, it is a metal-free electrocatalyst. On the contrary, the mass fraction of Fe in CS_7Fe–N lies in the middle of all samples. Nevertheless, CS_7Fe–N presents the highest ECSA and electrical conductivity, ultimately explaining the best performance in ORR of this electrocatalyst. Therefore, the quality (and not quantity) of Fe species seems to play a decisive role in governing the performance of the Fe–N-doped hollow CSs in ORR. X-ray photoelectron spectroscopy (XPS) was carried out to obtain additional insights on the type of Fe and N sites on the surface of the doped hollow CSs. However, surface Fe species were undetected through this technique (Table S4). This can be explained by the combination of the low amount of bulk Fe species (in the range 0.05–0.21 wt%, as determined by ICP-OES; Table S3) and possible carbon encapsulation of those Fe species. Regarding N species, no significant differences are observed among the Fe–N-doped hollow CSs (Fig. S2 and Table S4)), the presence of N in a chemical state like that of the Fe-N_x moiety in iron phthalocyanine [18] being confirmed for all the samples. Nevertheless, it is noteworthy that N-oxidized species (NO; corresponding to nitrogen oxides of N-pyridinic) were observed only for $CS_7Fe_{0.1}$-N. Additional insights on XPS analysis are provided in Section 3.2.2. Regarding structural defects and other crystal disorder assessed through Raman spectroscopy, CS_7Fe–N reveals an I_D/I_G ratio of 0.93, which is similar to that of bare CS_7 (I_D/I_G = 0.94; Fig. 3h). This allows concluding that the methodology used to incorporate Fe–N active sites does not induce additional structural defects in the carbon structure.

CS_7Fe–N reveals a stability to methanol cross-over significantly higher than that of Pt/C (Fig. 3i). In fact, the difference observed in the stability loss of CS_7Fe–N during 10000 s at 0.4 V *vs.* RHE in the absence (1%, cf. Table 2) and presence (5%, cf. Fig. 3i) of methanol amounts to 4%, whereas the relative current yielded by Pt/C decreases an additional 7% when methanol was added (from 8 to 15% stability loss, cf. Table 2 and Fig. 3i, respectively). Possible reasons behind the high activity and stability of CS_7Fe–N towards ORR will be addressed in the following section.

3.2.2. *Meticulous design of single-atom Fe–N active sites*

As discussed above, the performance of the Fe–N-doped hollow CSs in ORR seems to be governed by the quality of Fe species rather than the overall Fe load. Having that in mind, the procedure used for the synthesis of the sample with the highest activity for ORR (CS_7Fe–N) was deconstructed to study the importance and role of each precursor towards obtaining the optimized electrocatalyst. Accordingly, additional materials were prepared in the absence of glucose ($CS_7Fe\text{-}N_{No\ glucose}$), melamine ($CS_7$Fe), and Fe ($CS_7$–N); and employed in ORR. Clear differences can be identified in both the LSV curves (Fig. 4a) and the ORR performance indicators (Table 3). Single doping of CS_7 with N groups slightly shifts the ORR pathway towards the preferred direct four-electron pathway (Eq. (1)), as demonstrated by the lower H_2O_2 formation (20.6%) and higher n_e (3.6) obtained with CS_7–N when compared to the values obtained with CS_7 (41.7% and 3.2, respectively; Table 3). Nevertheless, E_{onset}, $E_{1/2}$, and J_L are negligibly affected by N-doping (Fig. 4a and Table 3). Additional insights regarding ORR mechanisms on N-containing carbon materials can be found elsewhere [6]. Likewise, single doping of CS_7 with Fe species slightly shifts the ORR pathway towards the preferred direct four-electron pathway (Eq. (1)). Indeed, the ORR performance indicators obtained with CS_7Fe are very similar to those obtained with CS_7–N (Table 3). The exception is J_L (4.07 mA cm^{-2}), which is higher than that obtained by both CS_7 (3.88 mA cm^{-2}) and CS_7–N (3.70 mA cm^{-2}; Fig. 4a and Table 3). ORR mechanisms on Fe-containing carbon materials have also been recently reviewed [7].

Implications of metal-carbon interactions in ORR are widely known [38]. In particular, heteroatoms with higher (N) or lower (B, and S) electronegativity than carbon can be used to modulate the charge density nearby the active sites and limit the agglomeration of metal precursors during the synthesis [11,39]. Having that in mind, CS_7 was doped with N and Fe simultaneously. The resulting material was denoted as $CS_7Fe\text{-}N_{No\ glucose}$. As observed, this approach effectively enhanced the performance in ORR (Fig. 4a and Table 3). Specifically, ORR on $CS_7Fe\text{-}N_{No\ glucose}$ proceeds almost exclusively through the preferred direct four-electron pathway (Eq. (1)), as demonstrated by the low H_2O_2 formation (8.0%) and high n_e (3.8) obtained (Table 3). Moreover, enhanced E_{onset} (0.90 V), $E_{1/2}$ (0.77 V), and J_L (4.49 mA cm^{-2}) are also obtained with $CS_7Fe\text{-}N_{No\ glucose}$ (Fig. 4a and Table 3), thus confirming the success of the synthesis methodology used for simultaneous doping of CS_7 with N and Fe species. Both ORR mechanisms and the nature of active sites of Fe–N-doped carbon materials have been the subject of a recent review [40].

Despite the high performance obtained with $CS_7Fe\text{-}N_{No\ glucose}$, additional efforts were made to improve catalyst design further. On that regard, glucose was already shown to act as a chelating agent during the synthesis of Fe–N-doped carbon materials, thus enhancing metal-

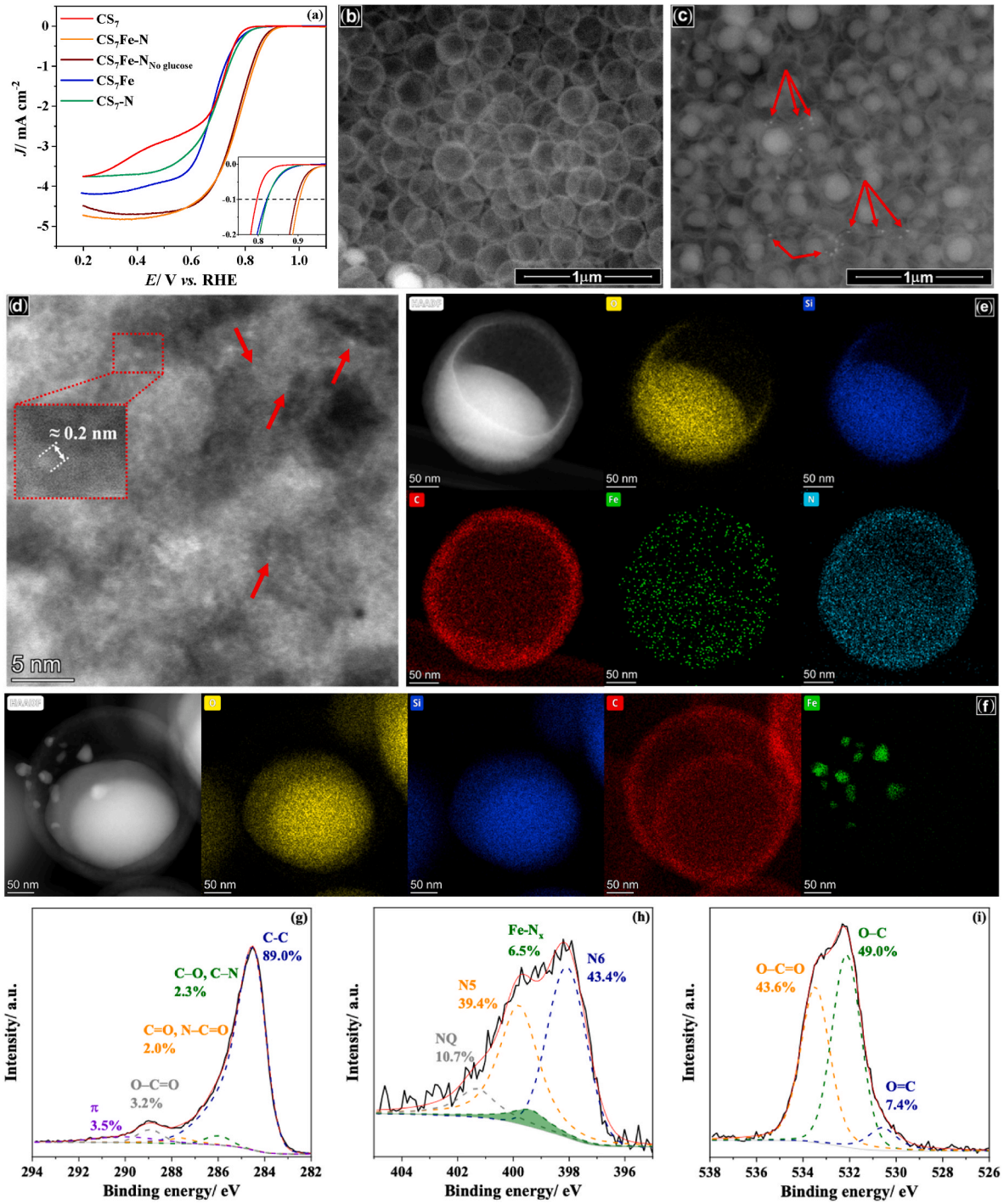

Fig. 4. (a) Linear sweep voltammetry (LSV) curves of hollow CSs prepared under different conditions, obtained in O_2-saturated 0.1 mol L^{-1} KOH at 1600 rpm; scanning electron microscopy (SEM) micrographs of (b) CS_7Fe–N and (c) CS_7Fe obtained in backscattered electron detection mode; (d) high-resolution transmission electron microscopy (HRTEM) micrograph of CS_7Fe–N; and scanning transmission electron microscopy-high angle annular dark field (STEM-HAADF) image and energy-dispersive X-ray spectroscopy (EDS) elemental maps of (e) CS_7Fe–N and (f) CS_7Fe (scale bar: 50 nm). Detailed X-ray photoelectron spectroscopy (XPS) spectra of the (g) C 1s, (h) N 1s, and (i) O 1s regions of CS_7Fe–N. Inset in (a) corresponds to a magnification of the region nearby onset potentials (E_{onset}). Red arrows in (c) point out to contrasts consistent with iron particles. O (yellow), Si (blue), C (red), Fe (green), and N (turquoise) are represented in the EDS elemental maps given in (e), whereas Si (blue), Fe (green), and C (red) are represented in the EDS elemental maps given in (f). Red arrows in (d) point out to contrasts consistent with Fe atoms. N6, Fe-N_x, N5, and NQ in (h) represent N-pyridinic, N in the chemical state similar to Fe-Nx moiety in iron phthalocyanine, N-pyrrolic, and N-quaternary species, respectively. (A colour version of this figure can be viewed online.)

heteroatom coordination and subsequent dispersion of active sites on the carbon surface [18]. Accordingly, CS_7Fe–N was synthesized as depicted in Fig. 1 and detailed in Section 2.2, *i.e.*, upon simultaneous doping CS_7 with N and Fe species in the presence of glucose. The performance of CS_7Fe–N in ORR is indeed better than that obtained with CS_7Fe-$N_{No\ glucose}$, although only slightly (Fig. 4a and Table 3). Slightly enhanced $E_{1/2}$ (0.79 V), J_L (4.68 mA cm^{-2}), H_2O_2 formation (6.9%), and n_e (3.9) are obtained with CS_7Fe–N when compared to CS_7Fe-$N_{No\ glucose}$ (0.77 V, 4.49 mA cm^{-2}, 8.0%, and 3.8, respectively; Table 3), confirming the beneficial role of adding glucose during the synthesis

Table 3
Summary of ORR results obtained with hollow CSs prepared under different conditions: onset potential (E_{onset}), half-wave potential ($E_{1/2}$), limiting current density (J_L), hydrogen peroxide (H_2O_2) formation, number of electrons transferred (n_e), and stability[a].

Sample	E_{onset}/ V	$E_{1/2}$/ V	J_L[b]/mA cm^{-2}	H_2O_2[c]/ %	n_e[b]	Stability[d]/ %
CS_7	0.81	0.74	3.88	41.7	3.2	89
CS_7Fe–N	0.90	0.79	4.68	6.9	3.9	99
CS_7Fe-$N_{No\ glucose}$	0.90	0.77	4.49	8.0	3.8	96
CS_7Fe	0.82	0.69	4.07	21.8	3.6	94
CS_7–N	0.82	0.72	3.70	20.6	3.6	99

[a] All data refers to experiments performed at 1600 rpm.
[b] Calculated at 0.2 V *vs*. RHE.
[c] Calculated at 0.4 V *vs*. RHE.
[d] Calculated after 10000 s at 0.4 V *vs*. RHE.

procedure.

In addition to ORR performance evaluation, relevant properties of the materials prepared to study the importance and role of each precursor towards obtaining the optimized electrocatalyst (CS_7Fe–N) were characterized. N_2 adsorption-desorption isotherms revealed similar textural properties among the materials under consideration (Fig. S3 and Table S5). The exception is CS_7Fe, with a better developed porosity. A negative correlation was found between the bulk Fe content (Table S5) and the performance of the hollow CSs prepared under different conditions, *i.e.*, the sample with the lowest bulk Fe content (CS_7Fe–N, with [Fe] = 0.12 wt%) is the best performing in ORR, followed by the samples with the second lowest (CS_7Fe-$N_{No\ glucose}$, with [Fe] = 0.27 wt%) and highest (CS_7Fe, with [Fe] = 0.32 wt%) Fe contents. Once again, these results confirm that the performance in ORR is dictated by the quality of Fe active sites on the carbon surface.

Despite the different bulk Fe loads, XRD patterns only reveal broad peaks at $2\theta \approx 23^o$ and very slight peaks at $2\theta \approx 44^o$ (Fig. S4), which are similar to those previously obtained with hollow CSs prepared with different Fe loads (Fig. 3f). Likewise, topographical characterization through SEM in secondary electron detection mode revealed very similar properties among the hollow CSs prepared under different conditions (Fig. S5), size included (Fig. S6). Nevertheless, differences become evident when SEM micrographs are obtained in backscattered electron detection mode (Fig. 4b and c). In the case of the CSs prepared in the absence of N precursor (CS_7Fe), Fe particles are observed even in a SEM micrograph obtained with low magnification (Fig. 4c). On the contrary, no contrasts corresponding to Fe particles are observed in the SEM micrograph of the Fe–N-doped CSs prepared in the presence of glucose (CS_7Fe–N; Fig. 4b). Nonetheless, the presence of Fe was confirmed by EDS in both cases (Fig. S7), together with C, Si, O, and, in the case of CS_7Fe–N, N. Moreover, SEM-EDS revealed no significant differences between the Fe–N-doped CSs prepared in the absence of glucose (CS_7Fe-$N_{No\ glucose}$; Fig. S8) and CS_7Fe–N (Figs. S7a and b).

The Fe-containing hollow CSs were also analyzed by TEM (Fig. S9). Micrographs obtained with low magnification enable similar observations to those obtained through SEM. Specifically, contrasts consistent with Fe particles are observed in the TEM micrograph of CS_7Fe (Fig. S9c); whereas only the contrasts arising from the presence of residual amounts of SiO_2 are observed in the TEM micrographs of CS_7Fe–N (Fig. S9a) and CS_7Fe-$N_{No\ glucose}$ (Fig. S9e). The porous structure of the Fe-containing hollow CSs becomes evident when TEM micrographs are collected with larger magnification (Figs. S9b, d, and f). HRTEM, STEM-HAADF, and EDS were also conducted on the hollow CSs. In this case, contrasts with *ca.* 0.2 nm and lower are observed in the HRTEM micrograph of CS_7Fe–N (Fig. 4d) despite the interference from SiO_2, which that can be attributed to the presence of single atoms of Fe. Additionally, Fe can be detected in these areas by EDS. Moreover, the STEM-HAADF image and EDS elemental maps of CS_7Fe–N show that the presence of O is associated with Si, whereas both Fe and N are extremely well dispersed on the carbon surface (Fig. 4e). Indeed, no Fe aggregates/particles are observed. On the contrary, Fe particles (diameter $\geq$ 10 nm) are clearly visible in the STEM-HAADF image and EDS elemental maps of CS_7Fe (Fig. 4f). Regarding the Fe–N-doped CSs prepared in the absence of glucose (CS_7Fe-$N_{No\ glucose}$), the observations obtained are very similar to those previously discussed for CS_7Fe–N. Contrasts consistent with Fe atoms (diameter $\approx$ 0.2 nm) are also observed in the HRTEM micrograph of CS_7Fe-$N_{No\ glucose}$ (Fig. S10a), whereas STEM-HAADF image and EDS elemental maps also confirm the association of O and Si, and the good dispersion of Fe and N on the carbon surface (Fig. S10b). Although slightly brighter/larger spots are apparently observed in some areas of the EDS Fe map of CS_7Fe-$N_{No\ glucose}$ (Fig. S10b) when compared to those obtained with CS_7Fe–N (Fig. 4e), this difference cannot be interpreted as a lower dispersion as it can just be the result of the higher Fe content quantified in the case of the former (Table S6). In any case, the Fe contents obtained by quantitative EDS analysis (Table S6) are always higher than the bulk Fe contents obtained by ICP-OES (Table S5).

XPS was carried out to obtain additional insights on the surface chemical environment of CS_7Fe–N. The deconvoluted C 1s spectrum reveals the typical configuration of a sp^2 hybridized carbon material, with the C–C peak corresponding to 89.0% of the overall carbon content (Fig. 4g). The analysis of the N 1s XPS spectrum reveals the existence of Fe-N_x coordination (Fig. 4h), thus confirming the presence of single-atom Fe–N active sites on the surface of the CS_7Fe–N electrocatalyst. In fact, 6.5% of its surface N content is coordinated to single-atom Fe in a chemical state like that of the Fe-N_x moiety in iron phthalocyanine [18], the remaining N being coordinated to carbon, as pyridinic- (N6; 43.4%), pyrrolic- (N5; 39.4%), and quaternary-N (NQ; 10.7%) species. N6 and NQ species have been shown to enhance the activity of metal-free ORR carbon electrocatalysts [41,42], which may explain the better results obtained with CS_7–N when compared to those obtained with bare CS_7 (Fig. 4a and Table 3). Nevertheless, the highest electrocatalytic enhancement occurs when single-atom Fe–N active sites are introduced, as observed when the ORR performance of CS_7Fe–N is compared to that of CS_7–N (Fig. 4a and Table 3). The O 1s XPS spectrum confirms the negligible presence of iron oxides on the surface of CS_7Fe–N, as no O–Fe peak was detected at *ca.* 529.5 eV (Fig. 4i). This observation agrees with the XRD data, in which no crystalline phases were observed for CS_7Fe–N (Fig. 3f). Therefore, the N 1s and O 1s XPS spectra of CS_7Fe–N suggest the predominance of single-atom Fe–N over other Fe species, as previously observed through electron microscopy techniques such as HRTEM (Fig. 4d) and STEM-HAADF/EDS (Fig. 4e). As described in Section 3.2.1, no Fe species were detected by XPS (ICP-OES confirmed a bulk Fe concentration as low as 0.12 wt%; *cf*. Table S3). Therefore, obtaining additional insights on Fe species by XPS is unfeasible. Nevertheless, the noticeable enhancement in ORR activity observed upon incorporation of such small iron load can be ascribed to the highly active single-atom Fe–N sites introduced on the surface of CS_7Fe–N.

A recent concern regarding the application of single-atom catalysts is aggregation and sintering during application in ORR, leading to poor stability [11]. It is thus noteworthy that CS_7Fe–N revealed a stability of 99% after 10000 s at 0.4 V *vs*. RHE (Table 3), a value superior to the 92% stability revealed by Pt/C – a commercial carbon black catalyst containing as much as 20 wt% of platinum (Table 2). In fact, CS_7Fe–N still yields a current density of 4.47 mA cm^{-2} after 24 h of continuous operation under those conditions (Fig. S11), corresponding to an electrocatalytic stability of 98%. This remarkable achievement may be ascribed to the high structural stability of the single-atom Fe–N active sites introduced on the surface of CS_7Fe–N.

3.2.3. *Computational studies*

DFT calculations were performed to obtain additional insights into the importance and role of each precursor towards obtaining the optimized electrocatalyst. Graphene nanoribbons share a carbon-based

composition similar to the structural elements of CS_7, making them suitable molecular models for theoretical investigations. Therefore, a graphene nanoribbon with 60 carbon atoms was used as the molecular model to simulate a graphene sheet in all the computational studies. The potential of employing a theoretical methodology at the nanoscale level for exploring larger molecules has been previously shown by our [43,44] and other [45,46] research groups. In fact, this computational strategy strikes a reasonable balance between the accuracy of the results and the computational resources required. Single-atom Fe, a cluster of 9 Fe atoms, and single-atom FeN_4 were considered as possible active sites, together with a bare graphene sheet. Schematic representations of the optimized structures obtained for the adsorption of O_2 on possible electrocatalytic active sites and Gibbs free energy diagrams of ORR through the associative four-electron pathway are given in Fig. 5. As observed, O_2 adsorption (*i.e.*, the first step of ORR) is most unfavored on a bare graphene sheet (Fig. 5i). A large reaction barrier is then observed for O_2 protonation to OOH* ($\Delta G = +4.33$ eV), thus rendering ORR through the direct four-electron pathway unfavorable under these conditions. These computational results agree with the experimental data obtained with CS_7; and explain the contribution of the indirect two-electron pathway when ORR is carried out on this metal-free material, as discussed in Section 3.1 ($n_e = 3.2$ and 41.7% of H_2O_2 formation; Table 3).

O_2 adsorption on the Fe-containing structures is more favorable ($4.98 \leq \Delta G \leq 5.49$ eV; Fig. 5j-l) than on bare graphene ($G = 6.69$ eV; Fig. 5i). Nevertheless, the most significant effects occur in the thermodynamical barriers for the subsequent steps of ORR. When the active site is a single-atom Fe, the limiting step is O_2 protonation to OOH* ($\Delta G = +1.54$ eV; Fig. 5j); whereas dissociation of OOH* to O* limits ORR on a small particle of Fe ($\Delta G = +1.74$ eV; Fig. 5k). Thus, one can conclude that single doping of CS_7 with Fe shifts the ORR pathway towards the preferred direct four-electron pathway, which agrees with the experimental results obtained with CS_7 and CS_7Fe (Section 3.2.2). It can also be concluded that single-atom Fe possesses higher electrocatalytic activity for ORR than a small Fe particle (9-Fe cluster). Nevertheless, the best performance is obtained with FeN_4. Indeed, all the elementary steps of ORR are thermodynamically favorable when proceeding on single-atom Fe coordinated to 4 atoms of N (Fig. 5l and Fig. S12). This significant decrease in the thermodynamical barrier for ORR can be ascribed to the ability of N atoms to limit the agglomeration of metal precursors such as Fe during the synthesis by anchoring individual metal centers and modulate the charge density nearby the active sites [11,39]. Indeed, such enhancement in ORR is consistent with the difference observed when the performances of CS_7Fe–N and CS_7Fe-$N_{No\ glucose}$ (*i.e.*, the N-containing hollow CSs; in which no Fe particles were identified through microscopy analyses, only contrasts consistent with Fe atoms being observed in the TEM micrographs depicted in Fig. 4d and g, respectively) are compared to that of CS_7Fe (*i.e.*, the sample prepared without N-doping; in which Fe particles clearly visible in the SEM micrograph depicted in Fig. 4c and the TEM micrograph depicted in Fig. S9c) in Fig. 4a and Table 3. Therefore, the computational results given in Fig. 5 suggest that single-atom Fe–N active sites were indeed introduced on the surface of CS_7Fe–N and CS_7Fe-$N_{No\ glucose}$, as also suggested through the experimental results discussed in Section 3.2.2.

4. Conclusions

Metal-free hollow CSs perform better than those still containing a SiO_2 core, suggesting the positive impact of the hollow structure for ORR. ORR on these metal-free catalysts proceeds both via direct (*i.e.*, four-electron) and indirect (*i.e.*, two-electron) reaction pathways. Nevertheless, electron rich regions caused by structural defects slightly shift the ORR pathway from the indirect two-electron to the preferred direct four-electron pathway (from n_e of 2.7–3.2.), thus yielding higher J_L.

Single-atom Fe–N active sites were introduced on the surface of the best-performing hollow CSs (*i.e.*, CS_7) without inducing additional structural defects on the carbon structure, demonstrating the feasibility of engineering such functionalities through a synthesis methodology employing only earth-abundant metal precursors such as iron (III) nitrate. Despite apparently being a simple synthesis methodology, only the proper understanding of each precursor's role allows achieving the goal.

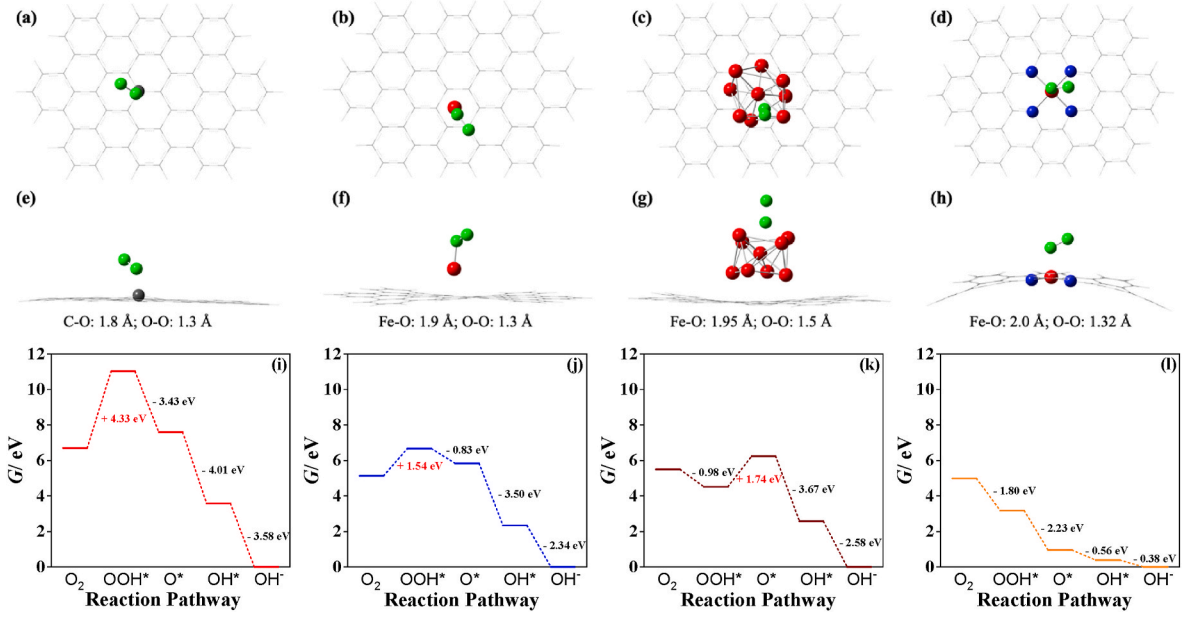

Fig. 5. (a–h) Schematic representation of the optimized molecular structures obtained for the adsorption of O_2 on possible electrocatalytic active sites on a graphene sheet: (a,e) bare graphene sheet, (b,f) single-atom Fe, (c,g) Fe cluster with 9 atoms, and (d,h) single-atom FeN_4. (a–d) front views, and (e–h) lateral views. (i–l) Gibbs free energy diagrams for the four-electron associative oxygen reduction reaction (ORR) on different electrocatalytic active sites on a graphene sheet: (i) bare graphene sheet, (j) single-atom Fe, (k) Fe cluster with 9 atoms, and (l) single-atom FeN_4. Colors in (a–h) represent O (green), Fe (red), N (dark blue), and C (gray). Values in (e–h) represent optimized distances between the represented atoms. Values inside (i–l) represent the overall Gibbs free energy change (ΔG) for each elementary step, at $U = 0$ V. (A colour version of this figure can be viewed online.)

Simultaneous incorporation of Fe and N precursors during the synthesis is crucial towards designing single-atom Fe active sites, as the performance in ORR is dictated by the quality (and not quantity) of Fe active sites on the carbon surface. Additional inclusion of glucose as chelating agent, together with Fe and N, leads to the slightly improved performance of the sample denoted as $CS_7Fe–N$ in ORR. Nevertheless, despite the thorough characterization performed, no significant differences were observed in the properties of the Fe–N-doped hollow CSs prepared in the absence and presence of glucose.

ORR on $CS_7Fe–N$ proceeds almost exclusively through the direct four-electron pathway ($n_e = 3.9$). A commercial carbon black catalyst containing as much as 20 wt% of platinum (Pt/C) revealed a similar feature, with $n_e = 3.9$. All this was accomplished despite the very low iron load introduced into $CS_7Fe–N$ (0.12 wt%). More interestingly, the stability of $CS_7Fe–N$ (both in the presence or absence of methanol) is higher than that of Pt/C. Therefore, although the activity of $CS_7Fe–N$ towards ORR is slightly inferior to that of the commercial Pt/C, $CS_7Fe–N$ outperforms Pt/C in what concerns to operating stability and methanol tolerance. Accordingly, the methodology herein reported opens a window of opportunity for the development of highly stable ORR electrocatalysts based on these unique hollow 3D carbon structures tailored with single-atom Fe–N active sites.

CRediT authorship contribution statement

Rui S. Ribeiro: Conceptualization, Methodology, Investigation, Formal analysis, Writing – original draft, Supervision. **Ana Luísa S. Vieira:** Investigation, Formal analysis, Writing – original draft. **Krzysztof Biernacki:** Methodology, Investigation, Formal analysis, Writing – review & editing. **Alexandre L. Magalhães:** Methodology, Writing – review & editing, Supervision. **Juan J. Delgado:** Methodology, Investigation, Formal analysis, Writing – review & editing. **Rafael G. Morais:** Methodology, Writing – review & editing. **Natalia Rey-Raap:** Conceptualization, Methodology, Writing – review & editing, Funding acquisition. **Raquel P. Rocha:** Conceptualization, Methodology, Writing – review & editing, Supervision, Project administration, Funding acquisition. **M. Fernando R. Pereira:** Conceptualization, Writing – review & editing, Supervision, Project administration, Funding acquisition.

Declaration of competing interest

The authors declare that they have no known competing financial interests or personal relationships that could have appeared to influence the work reported in this paper.

Acknowledgments

This work was financially supported by Projects PTDC/EQU-EQU/1707/2020 (“BiCat4Energy”), LA/P/0045/2020 (ALiCE), UIDB/50020/2020 and UIDP/50020/2020 (LSRE-LCM), funded by national funds through FCT/MCTES (PIDDAC), and HyGreen&LowEmissions (NORTE-01-0145-FEDER-000077), supported by Norte Portugal Regional Operational Programme (NORTE 2020), under the PORTUGAL 2020 Partnership Agreement, through the European Regional Development Fund (ERDF). RSR acknowledges FCT funding under Stimulus of Scientific Employment, Individual Support Call (CEEC IND) 5th Edition (2022.04079.CEECIND). RGM acknowledges the research grant from FCT (2020.06422.BD). Technical assistance with SEM and XPS, and XRD analyses is gratefully acknowledged to CEMUP and UME-UTAD teams, respectively.

Appendix A. Supplementary data

Supplementary data to this article can be found online at https://doi.org/10.1016/j.carbon.2023.118192.

References

[1] R. Ma, G. Lin, Y. Zhou, Q. Liu, T. Zhang, G. Shan, et al., A review of oxygen reduction mechanisms for metal-free carbon-based electrocatalysts, npj Comput. Mater. 5 (2019) 78, https://doi.org/10.1038/s41524-019-0210-3.
[2] C. Fu, C. Liu, T. Li, X. Zhang, F. Wang, J. Yang, et al., DFT calculations: a powerful tool for better understanding of electrocatalytic oxygen reduction reactions on Pt-based metallic catalysts, Comput. Mater. Sci. 170 (2019), 109202, https://doi.org/10.1016/j.commatsci.2019.109202.
[3] Y. Li, H. Dai, Recent advances in zinc–air batteries, Chem. Soc. Rev. 43 (2014) 5257–5275, https://doi.org/10.1039/C4CS00015C.
[4] M.K. Debe, Electrocatalyst approaches and challenges for automotive fuel cells, Nature 486 (2012) 43–51, https://doi.org/10.1038/nature11115.
[5] H.A. Firouzjaie, W.E. Mustain, Catalytic advantages, challenges, and priorities in alkaline membrane fuel cells, ACS Catal. 10 (2020) 225–234, https://doi.org/10.1021/acscatal.9b03892.
[6] R. Gutru, Z. Turtayeva, F. Xu, G. Maranzana, R. Thimmappa, M. Mamlouk, et al., Recent progress in heteroatom doped carbon based electrocatalysts for oxygen reduction reaction in anion exchange membrane fuel cells, Int. J. Hydrogen Energy 48 (2023) 3593–3631, https://doi.org/10.1016/j.ijhydene.2022.10.177.
[7] S.D. Bhoyate, J. Kim, F.M. de Souza, J. Lin, E. Lee, A. Kumar, et al., Science and engineering for non-noble-metal-based electrocatalysts to boost their ORR performance: a critical review, Coord. Chem. Rev. 474 (2023), 214854, https://doi.org/10.1016/j.ccr.2022.214854.
[8] K.C. Tsao, H. Yang, Oxygen reduction catalysts on nanoparticle electrodes, in: K. Wandelt (Ed.), Encyclopedia of Interfacial Chemistry, Elsevier, Oxford, 2018, pp. 796–811.
[9] M. Tahir, L. Pan, F. Idrees, X. Zhang, L. Wang, J.-J. Zou, et al., Electrocatalytic oxygen evolution reaction for energy conversion and storage: a comprehensive review, Nano Energy 37 (2017) 136–157, https://doi.org/10.1016/j.nanoen.2017.05.022.
[10] Y.-J. Wang, B. Fang, X. Wang, A. Ignaszak, Y. Liu, A. Li, et al., Recent advancements in the development of bifunctional electrocatalysts for oxygen electrodes in unitized regenerative fuel cells (URFCs), Prog. Mater. Sci. 98 (2018) 108–167, https://doi.org/10.1016/j.pmatsci.2018.06.001.
[11] S. Swain, A. Altaee, M. Saxena, A.K. Samal, A comprehensive study on heterogeneous single atom catalysis: current progress, and challenges, Coord. Chem. Rev. 470 (2022), 214710, https://doi.org/10.1016/j.ccr.2022.214710.
[12] Q. Liu, Y. Wang, Z. Hu, Z. Zhang, Iron-based single-atom electrocatalysts: synthetic strategies and applications, RSC Adv. 11 (2021) 3079–3095, https://doi.org/10.1039/D0RA08223F.
[13] T. Liu, L. Zhang, B. Cheng, J. Yu, Hollow carbon spheres and their hybrid nanomaterials in electrochemical energy storage, Adv. Energy Mater. 9 (2019), 1803900, https://doi.org/10.1002/aenm.201803900.
[14] G.A. Ferrero, K. Preuss, A. Marinovic, A.B. Jorge, N. Mansor, D.J.L. Brett, et al., Fe–N-doped carbon capsules with outstanding electrochemical performance and stability for the oxygen reduction reaction in both acid and alkaline conditions, ACS Nano 10 (2016) 5922–5932, https://doi.org/10.1021/acsnano.6b01247.
[15] C. Shu, Q. Tan, C. Deng, W. Du, Z. Gan, Y. Liu, et al., Hierarchically mesoporous carbon spheres coated with a single atomic Fe–N–C layer for balancing activity and mass transfer in fuel cells, Carbon Energy 4 (2022) 1–11, https://doi.org/10.1002/cey2.136.
[16] F. Zhang, Y. Zhu, Q. Lin, L. Zhang, X. Zhang, H. Wang, Noble-metal single-atoms in thermocatalysis, electrocatalysis, and photocatalysis, Energy Environ. Sci. 14 (2021) 2954–3009, https://doi.org/10.1039/D1EE00247C.
[17] A.L.S. Vieira, R.S. Ribeiro, A.R. Lado Ribeiro, A.M. Ribeiro, A.M.T. Silva, Hollow carbon spheres for diclofenac and venlafaxine adsorption, J. Environ. Chem. Eng. 10 (2022), 107348, https://doi.org/10.1016/j.jece.2022.107348.
[18] L. Zhao, Y. Zhang, L.-B. Huang, X.-Z. Liu, Q.-H. Zhang, C. He, et al., Cascade anchoring strategy for general mass production of high-loading single-atomic metal-nitrogen catalysts, Nat. Commun. 10 (2019) 1278, https://doi.org/10.1038/s41467-019-09290-y.
[19] R.S. Ribeiro, Z. Frontistis, D. Mantzavinos, D. Venieri, M. Antonopoulou, I. Konstantinou, et al., Magnetic carbon xerogels for the catalytic wet peroxide oxidation of sulfamethoxazole in environmentally relevant water matrices, Appl. Catal., B 199 (2016) 170–186, https://doi.org/10.1016/j.apcatb.2016.06.021.
[20] R.G. Morais, N. Rey-Raap, J.L. Figueiredo, M.F.R. Pereira, Fe, Co, N-doped carbon nanotubes as bifunctional oxygen electrocatalysts, Appl. Surf. Sci. 572 (2022), 151459, https://doi.org/10.1016/j.apsusc.2021.151459.
[21] N. Rey-Raap, E.G. Calvo, J.M. Bermúdez, I. Cameán, A.B. García, J.A. Menéndez, et al., An electrical conductivity translator for carbons, Measurement 56 (2014) 215–218, https://doi.org/10.1016/j.measurement.2014.07.003.
[22] M.J. Frisch, G.W. Trucks, H.B. Schlegel, G.E. Scuseria, M.A. Robb, J.R. Cheeseman, et al., Gaussian 09, Gaussian Inc., Wallingford, CT, 2016.
[23] A.D. Becke, Density-functional exchange-energy approximation with correct asymptotic behavior, Phys. Rev. A 38 (1988) 3098–3100, https://doi.org/10.1103/PhysRevA.38.3098.
[24] P.J. Stephens, F.J. Devlin, C.F. Chabalowski, M.J. Frisch, Ab initio calculation of vibrational absorption and circular dichroism spectra using density functional force fields, J. Phys. Chem. 98 (1994) 11623–11627, https://doi.org/10.1021/j100096a001.
[25] J. Tomasi, B. Mennucci, R. Cammi, Quantum mechanical continuum solvation models, Chem. Rev. 105 (2005) 2999–3094, https://doi.org/10.1021/cr9904009.
[26] J.K. Nørskov, J. Rossmeisl, A. Logadottir, L. Lindqvist, J.R. Kitchin, T. Bligaard, et al., Origin of the overpotential for oxygen reduction at a fuel-cell cathode, J. Phys. Chem. B 108 (2004) 17886–17892, https://doi.org/10.1021/jp047349j.

[27] J.K. Nørskov, T. Bligaard, J. Rossmeisl, C.H. Christensen, Towards the computational design of solid catalysts, Nat. Chem. 1 (2009) 37–46, https://doi.org/10.1038/nchem.121.
[28] Dennington Roy, Todd Keith, J. Millam, GaussView, Version 6.0, Semichem Inc., Shawnee Mission, KS, 2019.
[29] X. Ge, A. Sumboja, D. Wuu, T. An, B. Li, F.W.T. Goh, et al., Oxygen reduction in alkaline media: from mechanisms to recent advances of catalysts, ACS Catal. 5 (2015) 4643–4667, https://doi.org/10.1021/acscatal.5b00524.
[30] M. Florent, R. Wallace, T.J. Bandosz, Oxygen electroreduction on nanoporous carbons: textural features vs nitrogen and boron catalytic centers, ChemCatChem 11 (2019) 851–860, https://doi.org/10.1002/cctc.201801675.
[31] D. Barrera, M. Florent, K. Sapag, T.J. Bandosz, Insight into the mechanism of oxygen reduction reaction on micro/mesoporous carbons: ultramicropores versus nitrogen-containing catalytic centers in ordered pore structure, ACS Appl. Energy Mater. 2 (2019) 7412–7424, https://doi.org/10.1021/acsaem.9b01427.
[32] D. Deng, L. Yu, X. Pan, S. Wang, X. Chen, P. Hu, et al., Size effect of graphene on electrocatalytic activation of oxygen, Chem. Commun. 47 (2011) 10016–10018, https://doi.org/10.1039/C1CC13033A.
[33] R. Guidelli, R.G. Compton, J.M. Feliu, E. Gileadi, J. Lipkowski, W. Schmickler, et al., Defining the transfer coefficient in electrochemistry: an assessment (IUPAC Technical Report), Pure Appl. Chem. 86 (2014) 245–258, https://doi.org/10.1515/pac-2014-5026.
[34] S. Anantharaj, S. Noda, How properly are we interpreting the Tafel lines in energy conversion electrocatalysis? Mater. Today Energy 29 (2022), 101123 https://doi.org/10.1016/j.mtener.2022.101123.
[35] P. Hu, Y. Song, L. Chen, S. Chen, Electrocatalytic activity of alkyne-functionalized AgAu alloy nanoparticles for oxygen reduction in alkaline media, Nanoscale 7 (2015) 9627–9636, https://doi.org/10.1039/C5NR01376C.
[36] V.C.A. Ficca, C. Santoro, E. Placidi, F. Arciprete, A. Serov, P. Atanassov, et al., Exchange current density as an effective descriptor of poisoning of active sites in platinum group metal-free electrocatalysts for oxygen reduction reaction, ACS Catal. 13 (2023) 2162–2175, https://doi.org/10.1021/acscatal.2c05222.
[37] J. Du, Y. Zhang, H. Wu, S. Hou, A. Chen, N-doped hollow mesoporous carbon spheres by improved dissolution-capture for supercapacitor, Carbon 156 (2020) 523–528, https://doi.org/10.1016/j.carbon.2019.09.091.
[38] C. Durante, Metal–carbon interaction in metal nanoparticles and implication in the electrocatalysis of oxygen reduction, Curr. Opin. Electrochem. 36 (2022), 101119, https://doi.org/10.1016/j.coelec.2022.101119.
[39] Y. Yang, J. Fu, Y. Zhang, A.A. Ensafi, J.-S. Hu, Molecular engineering for bottom-up construction of high-performance non-precious-metal electrocatalysts with well-defined active sites, J. Phys. Chem. C 125 (2021) 22397–22420, https://doi.org/10.1021/acs.jpcc.1c07682.
[40] X. Zhang, L. Truong-Phuoc, T. Asset, S. Pronkin, C. Pham-Huu, Are Fe–N–C electrocatalysts an alternative to Pt-based electrocatalysts for the next generation of proton exchange membrane fuel cells? ACS Catal. 12 (2022) 13853–13875, https://doi.org/10.1021/acscatal.2c02146.
[41] G. Rambabu, Z. Turtayeva, F. Xu, G. Maranzana, M. Emo, S. Hupont, et al., Insights into the electrocatalytic behavior of nitrogen and sulfur co-doped carbon nanotubes toward oxygen reduction reaction in alkaline media, J. Mater. Sci. 57 (2022) 16739–16754, https://doi.org/10.1007/s10853-022-07653-3.
[42] Z. Duan, G. Henkelman, Identification of active sites of pure and nitrogen-doped carbon materials for oxygen reduction reaction using constant-potential calculations, J. Phys. Chem. C 124 (2020) 12016–12023, https://doi.org/10.1021/acs.jpcc.0c03951.
[43] I.S. Tavares, C.F.B.R. Figueiredo, A.L. Magalhães, The inner cavity of a carbon nanotube as a chemical reactor: effect of geometry on the catalysis of a Menshutkin S_N2 reaction, J. Phys. Chem. C 121 (2017) 2165–2172, https://doi.org/10.1021/acs.jpcc.6b08466.
[44] I. Alves, A.L. Magalhães, BN-doped graphene and single-walled carbon nanotubes for the catalysis of S_N2 reactions: insights from density functional theory modeling, J. Phys. Chem. A 123 (2019) 8188–8199, https://doi.org/10.1021/acs.jpca.9b05315.
[45] L. Huang, K. Zhong, Y. Wu, Y. Wu, X. Liu, L. Huang, et al., Facile synthesis of hollow carbon spheres by gas-steamed bifunctional NH_4F for efficient cathodes in microbial fuel cells, Carbon 207 (2023) 86–94, https://doi.org/10.1016/j.carbon.2023.02.062.
[46] Y. Jiao, Y. Zheng, M. Jaroniec, S.Z. Qiao, Origin of the electrocatalytic oxygen reduction activity of graphene-based catalysts: a roadmap to achieve the best performance, J. Am. Chem. Soc. 136 (2014) 4394–4403, https://doi.org/10.1021/ja500432h.